ACS APPLIED MATERIALS & INTERFACES

Research Article

www.acsami.org

Controlling the Formation of Rodlike V_2O_5 Nanocrystals on Reduced Graphene Oxide for High-Performance Supercapacitors

Meili Li,[†] Guoying Sun,*[,†] Pingping Yin,[†] Changping Ruan,[‡] and Kelong Ai*[,‡]

[†]Chemistry and Life Science School, Changchun University of Technology, 2055 Yanan Street, Changchun, People's Republic of China

[‡]State Key Laboratory of Electroanalytical Chemistry, Changchun Institute of Applied Chemistry, Chinese Academy of Sciences, 5625 Renmin Street, Changchun, People's Republic of China

Supporting Information

ABSTRACT: Vanadium pentoxide (V_2O_5) has attracted much attention for energy storage application because of its high Faradaic activity and stable crystal structure, which make it a promising electrode material for supercapacitors. However, the low electronic conductivity and small lithium-ion diffusion coefficient of V_2O_5 limit its practical applications. To overcome these limitations, a facile and efficient method is here demonstrated for the fabrication of V_2O_5/reduced graphene oxide (rGO) nanocomposites as electrode materials for supercapacitors. With this method, the reduction of graphene oxide can be achieved in a cost-effective and environmentally friendly solvent, without the addition of any other toxic reducing agent. Importantly, this solvent can control the formation of the uniform rodlike V_2O_5 nanocrystals on the surface of rGO. Compared to pure V_2O_5 microspheres, the V_2O_5/rGO nanocomposites exhibited a higher specific capacitance of 537 F g^{-1} at a current density of 1 A g^{-1} in neutral aqueous electrolytes, a higher energy density of 74.58 Wh kg^{-1} at a power density of 500 W kg^{-1}, and better stability even after 1000 charge/discharge cycles. Their excellent performances can be attributed to the synergistic effect of rGO and rodlike V_2O_5 nanocrystals. Such impressive results may promote new opportunities for these electrode materials in high-energy-density storage systems.

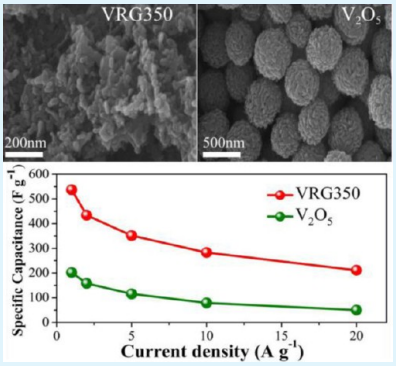

KEYWORDS: *graphene, V_2O_5, nanocomposites, electrode material, supercapacitors*

1. INTRODUCTION

Electrochemical capacitors, also known as supercapacitors or ultracapacitors, are a class of electrochemical energy storage devices that complement batteries.[1] They have received considerable attention worldwide because of their potentially high-impact characteristics including high power density (10 kW kg^{-1}), long cycle life (>10^5), high reliability, and low maintenance.[2] Such outstanding properties make them auspicious electrochemical energy storage devices in a wide range of applications, such as various portable electronic devices, hybrid motor vehicles, large industrial equipments, and military devices.[3] However, the energy stored in supercapacitors is currently 1 order of magnitude lower than that of batteries, which is still the greatest obstacle to the introduction of supercapacitors to some key applications that require high energy density.[4] Nowadays, commercially available supercapacitors are mainly based on porous activated carbon.[5] Unfortunately, their energy density is limited to about 4−5 Wh kg^{-1}, which is much lower compared to a lithium-ion battery (120−170 Wh kg^{-1}), lead acid cell (26−34 Wh kg^{-1}), and nickel metal hydride cell (40−100 Wh kg^{-1}).[3] As a consequence, the search for novel electrode systems with high energy density, high power density, and long cycle life is of great urgency and has stimulated extensive research.

Generally, supercapacitors can be classified into two types based on their charge-storage mechanism: electric double-layer capacitors (EDLCs) and pseudocapacitors.[6] In the EDLCs, the capacitance is dominated by the diffusion and accumulation of the electrostatic charge at the interface of electrolyte and the high-specific-area electrodes.[4] Such electrodes usually include active carbon, carbon nanotubes (CNTs), and graphene, which typically produce limited specific capacitance.[7] In the pseudocapacitance, nevertheless, most of the charge is stored through a fast redox reaction process on the surface of electrode materials, which may provide much higher specific capacitances (3−4 times higher than that of porous carbon).[1,8] Owing to higher energy density than those of electrochemical double-layer capacitive carbon materials, various pseudocapacitive transition-metal oxides and nitrides such as RuO_2,[9] MnO_2,[10] Co_3O_4,[11] NiO,[11,12] V_2O_5,[13] and vanadium nitride[14] have been extensively investigated as the electrode materials for supercapacitors. Among these, V_2O_5 is considered to be one of the most promising candidates because it possesses high energy density, natural abundance, low cost, a unique layered structure, mixed oxidation states (V^{2+}, V^{3+}, V^{4+}, and V^{5+}), and ease of

Received: September 4, 2013
Accepted: October 18, 2013
Published: October 18, 2013

synthesis.[15,16] Until now, several types of V_2O_5-based electrode materials have been reported for supercapacitors.[17−20] Nevertheless, these materials still suffered from poor electronic conductivities (10^{-2}−10^{-3} S cm^{-1}) and small lithium-ion diffusion coefficients (10^{-12}−10^{-14} cm^2 s^{-1}).[21]

The enhancement in the performance of supercapacitors can be achieved by two major approaches. The first tactic involves reducing the size of V_2O_5 materials to nanoscale because nanomaterials possess large surface area and short diffusion paths, which can provide more electrochemically active sites and alleviate the concentration polarization of electrode materials.[22] To date, different types of V_2O_5 nanostructures, such as nanorods,[23] nanofibers,[24] nanobelts,[25] nanowires,[26] and hollow microspheres,[27] have been demonstrated effective in improving the electrochemical kinetics, shortening the diffusion distance for Li^+ ions, compared with non-nanostructured materials. The introduction of electrically conductive materials into V_2O_5 should be taken into consideration as the second method for improving the performance of supercapacitors because these conductive materials can largely promote electronic transport. In previous studies, several types of conductive materials, such as CNT, mesoporous carbon, graphene, and conductive polymer, have been investigated as the supports to produce V_2O_5-based nanocomposites. Among them, graphene is preferable to replace other carbon matrixes because of its extraordinary properties including high electrical conductivity, unusual mechanical strength, and ultralarge specific surface area.[28] As a consequence, a number of graphene/metal oxide nanocomposites have been reported as electrode materials for energy storage, such as graphene/RuO_2,[29] graphene/MnO_2,[30] graphene/polymer,[31] graphene/V_2O_5,[32,33] and graphene/$Ni(OH)_2$.[34] Despite an enhanced electrochemical performance, we believe there is still considerable room for improving the synthesis and properties of electrode materials for supercapacitors.

In this paper, we demonstrate a facile and efficient method for controlling the formation of rodlike V_2O_5 nanocrystals on reduced graphene oxide (rGO) for high-performance supercapacitors. Different from the previously reported works, our method has at least two advantages: (1) it does not need a complex experimental procedure; (2) the formation of uniform V_2O_5 nanorods on the surface of rGO can be controlled simply by an environmentally friendly and cost-effective solvent, ethanol, and well-dispersed V_2O_5 nanorods on the surface of rGO can effectively inhibit the agglomeration and restacking of rGO sheets.[35] This method sufficiently utilizes the synergistic effects of the high electrochemical performance of V_2O_5 nanorods and the high conductivity of rGO. When employed as an electrode material for supercapacitors, the resulting V_2O_5/rGO nanocomposites can exhibit high specific capacitance, high energy density, and good stability. This discovery may promote these nanocomposites as high-performance electrode materials in supercapacitors.

2. EXPERIMENTAL SECTION

2.1. Preparation of Graphene Oxide (GO) Nanosheets. GO nanosheets were prepared by chemical exfoliation of graphite power according to a modified Hummer's method.[36] Briefly, exfoliation of nanosheets was achieved under ultrasonic treatment for 60 min (1000 W, 20% amplitude). Subsequently, the obtained brown dispersion was subjected to 5 min of centrifugation at 3000 rpm to eliminate a black precipitate, and the residual solution was used to form a homogeneous GO aqueous dispersion (2 mg mL^{-1}) for further experiments and characterization.

2.2. Preparation of Rodlike V_2O_5 Nanocrystals on rGO. The synthesis was carried out via solvothermal treatment and a subsequent annealing process. In a typical experiment, 25 mg of GO sheets was washed three times with anhydrous ethanol by ultrasonication and centrifugation. Then, it was dispersed fully into 40 mL of an anhydrous ethanol solution and ultrasonicated for another 40 min. After that, 300 μL of vanadium oxytripropoxide (VOTP; 99% purity, Aldrich) was added dropwise into the above GO solution under magnetic stirring. Finally, the resulting mixed solution was transferred into a 100-mL Teflon-lined stainless steel autoclave and kept in an electric oven at 160 °C for 24 h. The autoclave was then taken out of the oven and left to cool naturally to room temperature. By this solvothermal treatment, the reduction of GO to graphene and the growth of V_xO_y nanoparticles can be simultaneously achieved. The as-prepared V_xO_y nanoparticles on rGO (denoted as VRG) were washed several times with ethanol and then dried in an electric oven at 60 °C for 10 h. The final V_2O_5/graphene nanocomposites were obtained by annealing of VRG at different temperature from 250 to 550 °C for 0.5 h, with a heating rate of 10 °C min^{-1} in air.

Different amounts of VOTP (100, 200, 300, 500, and 700 μL) were added into the GO solution to investigate the effect of structures and morphologies on the electrochemical performance. Furthermore, experiments using ammonium metavanadate (NH_4VO_3, AM) as the precursor [AM was dissolved in deionized (DI) water (2 mL) in the presence of HCl (2 mL, 2M)] or using DI water as the solvent were carried out by the same method. Finally, unsupported pure V_2O_5 microspheres were also prepared following a procedure similar to that of VRG350 by replacing GO with 2 mL of distilled water, which was added dropwise to allow slow hydrolysis of VOTP.

2.3. Characterization. Transmission electron microscopy (TEM) images were taken using a TECNAI G2 high-resolution transmission electron microscope with an accelerating voltage of 200 kV. All TEM samples were created by depositing a drop of diluted suspensions in ethanol on a carbon-film-coated copper grid. The scanning electron microscopy (SEM) measurement of the samples was carried out using a FEI/Philips XL30 ESEMFEG field-emission scanning electron microscope. In addition, elemental analysis was performed on a Vario EL cube (Elementar Analysensysteme GmbH) to determine the carbon content of the samples. X-ray diffraction (XRD) spectra were obtained through a Bruker D8 ADVANCE diffractometer (Germany) using Cu Kα (1.5406 Å) radiation. X-ray photoelectron spectroscopy (XPS) measurement was performed on an ESCALAB-MKII spectrometer (VG Co. United Kingdom) with Al Kα radiation as the X-ray source for excitation. Fourier transform infrared (FTIR) spectra were collected on a VERTEX 70 FTIR spectrometer (Bruker). Raman analysis was carried out on lab RAM ARAMIS Raman spectrometer with 785 nm wavelength incident laser light. Nitrogen adsorption and desorption isotherms were measured at 77 K with a Quadrachrome Adsorption Instrument.

2.4. Electrochemical Measurements. The electrochemical data were collected under an electrochemical cell of both three-electrode and symmetric two-electrode systems. A suspension of the as-prepared materials with a concentration of 2.0 mg mL^{-1} was prepared by ultrasonically dispersing them (5 mg) into a mixture solution (2.5 mL) of ethanol, water, and Nafion. The suspension (5 μL) was then dropped onto the glassy carbon electrode and dried thoroughly in air. The glassy carbon electrode coated with the as-prepared materials was used as the working electrode. The reference and counter electrodes were Ag/AgCl and Pt, respectively. We selected a 8 M LiCl solution (Tianjin Fu Chen Chemical Reagent Factory, 95%) as the electrolyte because of its high solubility in vanadium oxide and low specific capacitance in other aqueous electrolytes[37] (see Table S1 in the Supporting Information). Cyclic voltammetry (CV) and galvanostatic charge/discharge curves were measured by a CHI 660D electrochemical workstation (Shanghai CH Instruments Co., China), with the potential being swept from −0.3 to +0.7 V for the three-electrode system (from −0.6 to +0.6 V for the symmetric two-electrode system). Electrochemical impedance spectroscopy (EIS) measurements were carried out with a Solartron 1255B frequency response analyzer (Solartron Inc.). All supercapacitors were tested in the following order

to ensure reproducibility and accuracy: CV (at scan rates increasing from 50 to 350 mV s^{-1}) was followed by C–D (at current density increasing from 1 to 20 A g^{-1}) and EIS (at frequencies decreasing from 100 kHz to 0.05 Hz). In the three-electrode system, the specific capacitance was calculated according to the equation

$$C = \frac{I\Delta t}{m\Delta V} \quad (1)$$

where I is the discharge current (A), Δt is the discharge time, m is the total mass of active material, and ΔV is the discharge voltage. The energy and power densities were estimated from charge/discharge curves by the equations

$$E = \frac{C(\Delta V)^2}{2} \quad (2)$$

$$P = \frac{Q\Delta V}{2t} = \frac{E}{t} \quad (3)$$

where E is the average energy density (Wh kg^{-1}), C is the specific capacitance based on the total mass of active material (F g^{-1}), ΔV is the potential window of discharge (V), P is the average power density (W kg^{-1}), Q is total charge delivered (C), and t is the discharge time (s).

3. RESULTS AND DISCUSSION

3.1. Preparation and Characterization of V_2O_5/Graphene Nanocomposites. V_xO_y nanoparticles on rGO (denoted as VRG) were prepared by hydrolyzing VOTP in ethanol at 160 °C in the presence of GO. Subsequent annealing of VRG in air at 350 °C led to the formation of uniform V_2O_5-rGO-350 °C (abbreviated to VRG350) nanocomposites. In this case, VOTP, GO, and ethanol were chosen as starting materials based on the following consideration. First, GO can be introduced to abundant functional groups, such as hydroxyl, carboxyl, and carbonyl, by a modified Hummer's method.[36] These functional groups can greatly facilitate the dispersion of GO, and they also provide the centers of polymerization and condensation for $[VO(OH)_3]$, which formed during slow hydrolysis of VOTP.[38] $[VO(OH)_3]$ was anchored onto the rGO surface through the nucleophilic addition of a hydroxyl group followed by coordination expansion and condensation processes, thus resulting in the grafting of V_xO_y layers onto the rGO surface.[39,40] Second, the type of vanadium source is a critical factor for the formation of VRG nanocomposites. For comparison purposes, AM was used to replace VOTP, and the experimental results show that only pure rGO was obtained (see Figures S1a,b and S2a,b in the Supporting Information). During the hydrolysis process, AM would produce excess acidic groups, which would form electrostatic repulsion with the electronegative groups on the surface of GO. As a result, AM could not be readily grafted onto the surface of GO. Third, because of fast hydrolysis of VOTP in aqueous solution, the neutral products $[VO(OH)_3]$ could form vanadium oxide immediately and result in bulk aggregation (see Figures S1c,d and S2a–c in the Supporting Information). Therefore, ethanol was used to slow the hydrolysis rate of VOTP. This would facilitate $[VO(OH)_3]$ to react well with the functional group (OH) on the surface of GO, and the uniform nanocomposite VRG was obtained. In addition, under environments of high temperature and high pressure, ethanol was capable of reducing GO to rGO,[41] which is necessary to improve the conductivity of VRG nanocomposites.

The morphology of VRG350 was elucidated by SEM and TEM. As shown in the low-magnification SEM, multilayer assemblies of V_2O_5 nanoparticles were anchored and uniformly distributed on the surface of rGO sheets (Figure 1a). The SEM image with a higher magnification (Figure 1b) revealed that the

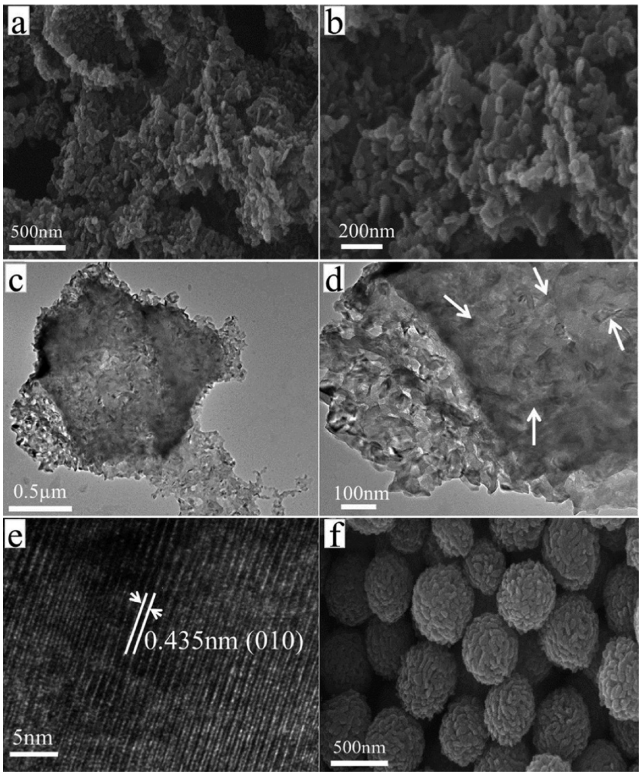

Figure 1. (a and b) SEM, (c and d) TEM, and (e) HRTEM images of VRG350. (f) SEM image of pure V_2O_5 microspheres.

surface of rGO was covered with small nanorods with lengths of around 60–100 nm and diameter of about 15 nm, which would provide a unique structure and a short diffusion path for an electrolyte ion.[42] The rodlike V_2O_5 nanostructure was also confirmed by TEM, and these nanorods were still anchored on rGO even after long-time sonication (Figure 1c,d), implying the strong interaction between V_2O_5 and rGO sheets.[35] The high-resolution TEM (HRTEM) image of these small nanorods exhibited well-defined lattice spacing of ca. 0.435 nm, corresponding to the (010) plane of a V_2O_5 crystal (Figure 1e). For comparison, a control experiment was performed in the absence of GO. The SEM image indicated that highly uniform microspheres with diameter of around 600–700 nm were obtained (Figure 1f). The structure of these microspheres was further investigated by TEM and HRTEM (see Figure S3a,b in the Supporting Information). Furthermore, the doping nature in VRG350 can be unraveled by a high-angle annular dark-field scanning TEM (HAADF-STEM) image of carbon and vanadium (Figure 2a). As expected, vanadium was uniformly distributed on rGO, which can availably restrain the agglomeration and restacking of rGO. However, carbon was also observed in pure V_2O_5 microspheres (Figure 2b), possibly because of the incomplete decomposition of the precursor at 350 °C. Elemental analysis revealed that the content of carbon is 7.96% and 0.04% in VRG350 and pure V_2O_5, respectively (see Table S2 in the Supporting Information).

Subsequently, typical XRD patterns of these crystalline-phase products were identified. The characteristic peaks in the XRD patterns of VRG350 and pure V_2O_5 samples can be unambiguously indexed to the orthorhombic V_2O_5 phase

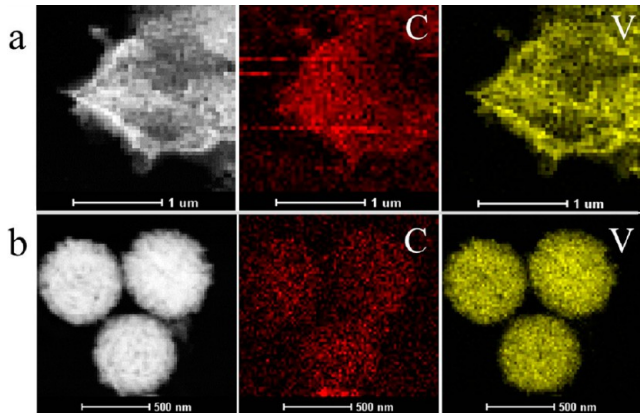

Figure 2. (a and b) HAADF-STEM images of VRG350 and pure V_2O_5 microspheres combined with EDS mapping in the same area and the relative intensities of carbon (red) and vanadium (yellow) elements.

(JCPDS card no. 01-0359, space group *Pmmn*, a = 11.48 Å, b = 4.36 Å, and c = 3.55 Å),[43] and no other impurity peaks were detected (Figure 3a). It is interesting that the conventional stacking peak of graphene nanosheets, usually located at ca. 26°, was not detected in VRG350 composites, possibly resulting from the formation of uniform V_2O_5 nanorods on rGO sheets.[11] To further investigate the chemical states of vanadium and the reduction degree of GO in the nanocomposites, XPS

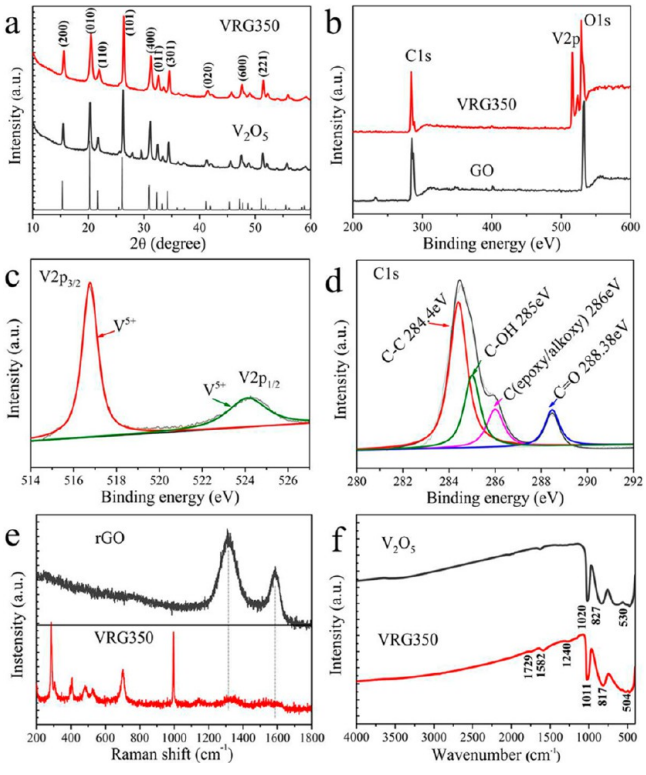

Figure 3. (a) XRD patterns of pure V_2O_5 microspheres and VRG350 nanocomposites. (b) Survey XPS spectrum showing C 1s, V 2p, and O 1s emanating from the VRG350 nanocomposites. (c) XPS spectrum of the V 2p binding energy region showing spin−orbit splitting of $2p_{3/2}$ and $2p_{1/2}$. (d) C 1s spectra for the VRG350 nanocomposites. (e) Raman spectra of the rGO sheets and VRG350 nanocomposites. (f) FTIR spectrum of pure V_2O_5 microspheres and VRG350 nanocomposites.

was carried out. The survey spectrum of VRG350 nanocomposites mainly shows carbon, oxygen, and vanadium species (Figure 3b). Besides, higher-resolution spectra were also recorded to understand the electronic states of the elements. In the V 2p spectrum (Figure 3c), two major peaks are V $2p_{3/2}$ and V $2p_{1/2}$ with binding energies at 516.73 and 524.12 eV,[44,45] implying the formation of a V_2O_5 phase in the nanocomposite matrix. Furthermore, a detailed analysis of the C 1s region indicated that it can be further divided into four peaks, which were located at 284.4, 285.0, 286.0, and 288.4 eV and assigned to C−C/C═C, C−OH, C (epoxy and alkoxy), and C═O groups (Figure 3d).[46] Compared to GO (see Figure S4a in the Supporting Information), the peaks related to C−O (epoxy and alkoxy) were much weaker, revealing that most of the oxygen-containing functional groups were removed after reduction.[47] However, the intensity of the C−OH peak (285 eV) is higher than that of GO, which may be due to the vanadium bound to the surface of rGO. Therefore, the XPS results further revealed that the product of VRG350 is indeed composed of rGO and V_2O_5.

The Raman spectra of rGO and VRG350 are shown in Figure 3e. VRG350 exhibited bands at 284, 306, 406, 483, 525, 702, and 996 cm^{-1}, which were characteristic modes for V_2O_5.[48] Moreover, there are two broad peaks at 1319 and 1585 cm^{-1} in the VRG350 nanocomposites, corresponding to the D and G bands of rGO, respectively. The G band represents the in-plane bond-stretching motion of the pairs of C sp^2 atoms (the E_{2g} phonons), whereas the D band corresponds to the breathing modes of rings or κ-point phonons of A_{1g} symmetry.[49] FTIR spectroscopy of VRG350 nanocomposites and pure V_2O_5 microspheres was performed over the range of 400−4000 cm^{-1} (Figure 3f). The band at 1011 cm^{-1} was associated with the V═O stretching vibration.[50] The bands at 817 and 504 cm^{-1} correspond to the V−O−V bending vibration and edge-sharing vibration, respectively.[50] A red shift of the characteristic band at 1011 cm^{-1} was observed for VRG350 composites, which may be attributed to the interaction of rGO with the vanadyl groups of V_2O_5. In addition, for GO (see Figure S4b in the Supporting Information), the spectrum exhibited the characteristic peaks of O−H (ν_{O-H} at 3435 cm^{-1}), C═O ($\nu_{C=O}$ at 1717 cm^{-1}), C═C ($\nu_{C=C}$ at 1568 cm^{-1}), and C−O (ν_{C-O} at 1187 cm^{-1}). The FTIR spectrum of VRG350 showed significant differences from that of GO. There was an obvious decrease in the intensities of the characteristic absorption bands of oxygen functionalities (ν_{O-H}, $\nu_{C=O}$, and ν_{C-O}),[51] suggesting that GO had been successfully reduced to graphene.

3.2. Optimization of the Annealing Temperature. Prior to using the products as electrode materials for supercapacitors, we first optimized the annealing temperatures. The morphology of VRG nanocomposites was investigated by SEM. It can be seen that the flowerlike V_xO_y nanoparticles were anchored onto the surface of rGO sheets in the low-magnification SEM image (Figure 4a). The high-magnification image (Figure 4b) shows that VRG was covered with uniform nanoparticles. When the as-prepared VRG was annealed at 250 °C (VRG250), flowerlike V_xO_y nanoparticles disappeared and aggregated on rGO sheets, as observed in Figure 4c. While the annealing temperature increased from 350 to 550 °C, V_xO_y nanoparticles grew into rodlike V_2O_5, and the average length changed from ~100 to ~680 nm with diameter ranging from 15 to 120 nm (Figure 4d−f). The CV and galvanostatic charge/discharge experiments revealed that VRG350 had the largest encircled

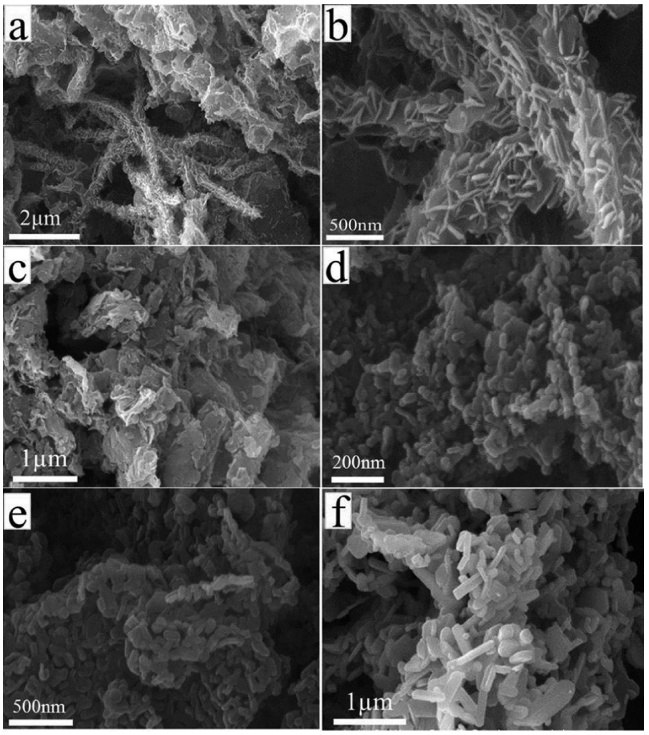

Figure 4. Typical SEM images of (a and b) VRG, (c) VRG250, (d) VRG350, (e) VRG450, and (f) VRG550.

area and longest discharge time, implying that VRG350 had the best capacitance behavior (Figure 5).[52] The specific capacitance

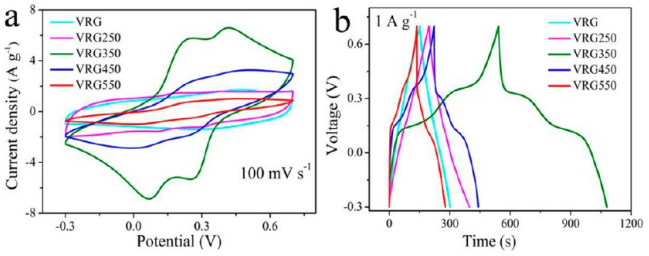

Figure 5. (a) CV curves at a sweep rate of 100 mV s^{-1} and (b) galvanostatic charge/discharge curves at a constant current density of 1 A g^{-1} for as-prepared samples at different temperatures.

of VRG350 was calculated to be 537 F g^{-1} at a current density of 1 A g^{-1} in a 8 M LiCl solution, higher than that of VRG (149 F g^{-1}), VRG250 (200.7 F g^{-1}), VRG450 (220.2 F g^{-1}), and VRG550 (141.3 F g^{-1}). We further investigated the electrochemical performances of VRG300 (333 F g^{-1}) and VRG400 (419 F g^{-1}), which are both lower than that of VRG350 (see Figure S5 in the Supporting Information). Consequently, the optimized annealing temperature was 350 °C for the obtained nanocomposites.

To ascertain the origin of the excellent electrochemical behavior of VRG350, the crystallographic structures of the as-prepared samples were investigated by XRD (Figure 6a). The absence of sharp diffraction peaks and the weak intensity of the XRD patterns for VRG and VRG250 imply their poor crystallinity.[32] By contrast, when the annealing temperature was increased to 350 °C, the diffraction peaks of the as-prepared samples increased remarkably and matched well with the crystal structure of the orthorhombic V_2O_5 phase,

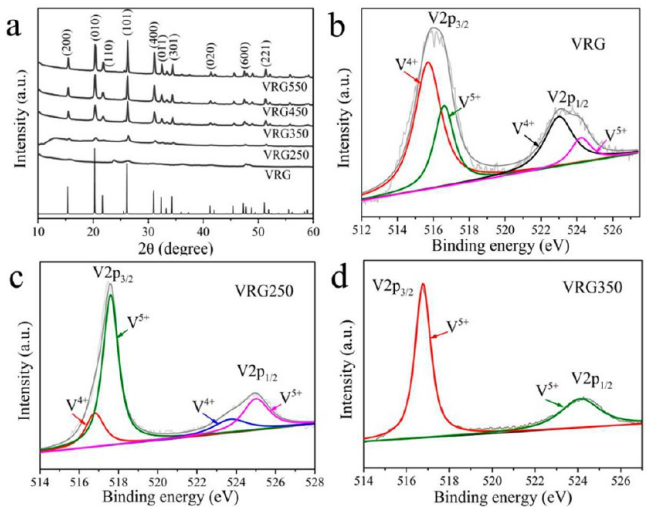

Figure 6. (a) XRD patterns of the different samples. The higher-resolution XPS spectra of V 2p for (b) VRG, (c) VRG250, and (d) VRG350.

confirming their good crystallinity. XPS was also conducted to analyze the chemical state of vanadium for the obtained samples. Higher-resolution spectra of VRG and VRG250 are displayed in Figure 6b,c. The broad peaks of V $2p_{3/2}$ and V $2p_{1/2}$ can be deconvoluted into two peaks corresponding to V^{4+} and V^{5+} states, respectively[53] (Figure 6b). Compared with VRG, the ratio of V^{4+}/V^{5+} is lower for VRG250. When the annealing temperature was increased to 350 °C, the peak of V^{4+} disappeared, suggesting that the product obtained at 350 °C had been transformed into V^{5+} completely (see Figures 6d and S6 in the Supporting Information). Previous reports demonstrated that V^{5+} could generate charges and create pseudocapacitance by multiple redox reactions.[54] Consequently, there is a good reason for the higher specific capacitance of VRG350 than that of VRG and VRG250. However, it could not explain the reason of the low capacitance for VRG450 and VRG550. Inspired by this, we turned to investigating the content of carbon and vanadium for different samples (see Table S2 in the Supporting Information). Elemental analysis manifested that the content of carbon was very low for VRG450 (0.26%) and VRG550 (0.17%). Hence, we concluded that the low capacitance of VRG450 and VRG550, compared with that of VRG350, might attribute to pyrolysis of the carbon skeleton, resulting in poor electronic conductivity of the nanocomposites. Therefore, the higher capacitance of the VRG350 electrode can be ascribed to the synergistic effect of rGO and rodlike V_2O_5 nanocrystals. First, rGO sheets enhance the electronic conductivity of the overall electrode and contribute electric double-layer capacitance. Second, those small well-dispersed V_2O_5 nanorods on rGO sheets can effectively utilize their high pseudocapacitance.[34] Third, the rGO sheets not only protect V_2O_5 against disintegration but also buffer the strain aroused by the volume expansion during the charging and discharging processes.[55] Finally, the strong adhesion between V_2O_5 nanorods and rGO sheets may facilitate fast electron transfer through the highly conductive rGO sheets, leading to enhancement of the electrochemical performance.[35]

3.3. Optimization of Vanadium Loading on rGO. The effect of the vanadium content in the obtained nanocomposites on their electrochemical behavior was investigated by loading different amounts of vanadium on rGO sheets. Figure 7 shows

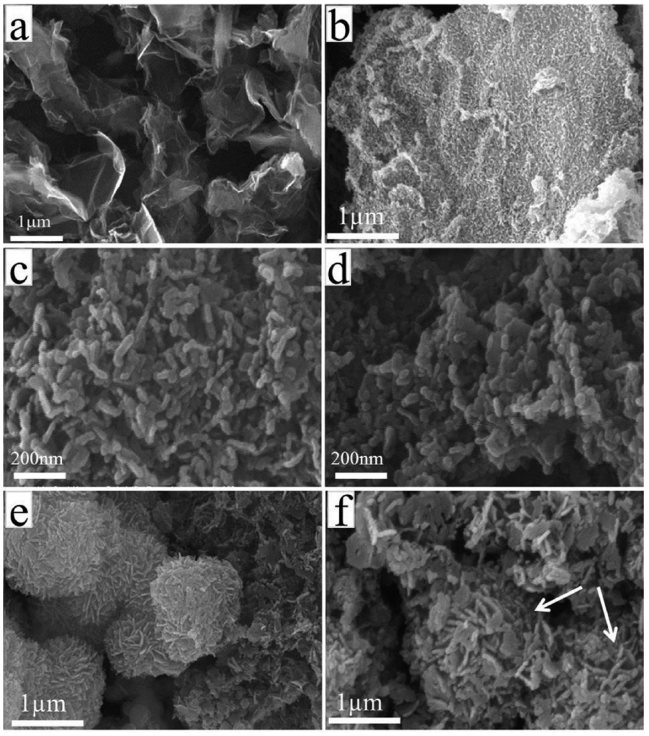

Figure 7. SEM images for as-prepared samples with different mass ratios of VOTP to GO: (a) GV_0; (b) GV_4; (c) GV_8; (d) GV_{12}; (e) GV_{22}; (f) GV_{30}.

the SEM images of VRG350 nanocomposites with different mass ratios of VOTP to GO. Compared with GV_0 (the mass ratio of VOTP to GO is 0, denoted as GV_0; Figure 7a), the SEM study of GV_4 showed that V_2O_5 nanoparticles uniformly distributed on the rGO surface in the low-magnification image (Figure 7b). In the high-magnification image, these nanoparticles present rodlike morphology with a length of around 50 nm (see Figure S7a in the Supporting Information). As shown in Figure 7c,d, when the mass ratio of VOTP to GO was 8−12, the V_2O_5 nanorods displayed similar morphology, around 15 nm width and 60−100 nm length. A close examination of GV_{12} revealed that the surface of these nanorods is rough and there are a lot of small bumps (see Figure S7b in the Supporting Information). However, when the amount of VOTP was sufficient (GV_{22} and GV_{30}), the self-assembly of these V_2O_5 nanorods occurred to form microspheres based on an oriented aggregation mechanism[56] (Figure 7e,f). Apparently, this result was due to the relative decrease of rGO sheets, which act as the support for the deposition of V_2O_5 nanorods. CV and galvanostatic charge/discharge curves for the as-synthesized products with different mass ratios of VOTP to GO are shown in Figure 8a,b. GV_0 and GV_{30} showed the lowest current output, suggesting that it was necessary to optimize the ratio of vanadium to carbon to overcome the poor electric double-layer capacitance of rGO and the low electronic conductivity of V_2O_5. Compared with GV_4, GV_8, and GV_{22}, GV_{12} exhibited the highest current output and the longest discharge time. The specific capacitance of GV_{12} calculated from the discharge curves is 537 F g^{-1} at a current density of 1 A g^{-1} in a 8 M LiCl solution, higher than that of GV_0 (63 F g^{-1}), GV_4 (333 F g^{-1}), GV_8 (420 F g^{-1}), GV_{22} (324F g^{-1}), and GV_{30} (246 F g^{-1}). This result indicated that GV_{12} realized the sufficient utilization of active materials. Simultaneously, the

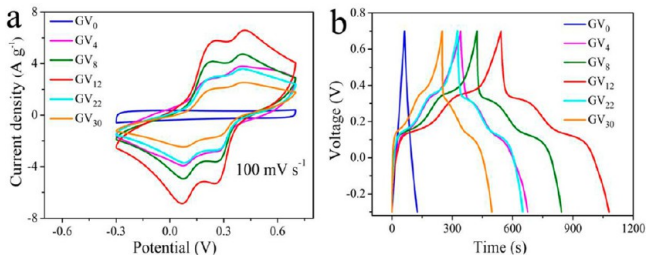

Figure 8. (a) CV curves at a sweep rate of 100 mV s^{-1} and (b) galvanostatic charge/discharge curves at a current density of 1 A g^{-1} for as-prepared samples with different mass ratios of VOTP to GO.

higher specific capacitance was also derived from a high faradaic capacitance, short ion diffusion, and electron transportation distance.[42] We performed Brunauer−Emmett−Teller (BET) surface area, elemental, and EIS analysis for the different samples to prove the above results (see Tables S3 and S4 and Figure S8 in the Supporting Information).

3.4. Electrochemical Properties of VRG350. To evaluate the capacitive behavior of our optimized products (VRG350 with GV_{12}), CV was carried out with a three-electrode system in a 8 M LiCl solution. As indicated in Figure 9a, the encircled

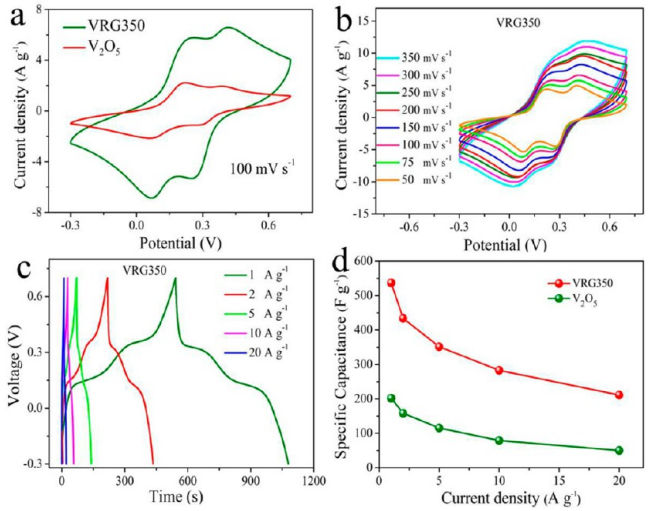

Figure 9. (a) CV curves at a scan rate of 100 mV s^{-1} for VRG350 and pure V_2O_5 microspheres. (b) CV diagrams at different sweep rates. (c) Galvanostatic charge/discharge curves at different current densities for the VRG350 electrode. (d) Specific capacitance of VRG350 and pure V_2O_5 microspheres as a function of the different current densities based on the charge/discharge curves.

area of the CV curve, which can be used to estimate the capacitance, was around 2.5-fold larger than that of pure V_2O_5 microspheres. There are probably two main reasons for this. First, the introduction of rGO enhanced the electrical conductivity of the overall electrode. Second, these nanocomposites possessed a larger surface area (49.16 m^2 g^{-1}) than that of pure V_2O_5 microspheres (37.57 m^2 g^{-1}) (see Figure S9 in the Supporting Information), which should further increase their electrochemical capacitance. Compared with electric double-layer capacitance, most of Faradaic redox reactions would present large redox current peaks.[57] It is observed that a pair of strong redox peaks appeared for VRG350 composites (Figure 9a), thus indicating that the capacitance characteristics of VRG350 composites were mainly induced by Faradaic redox

reactions. When the scan rates were increased from 50 to 350 mV s^{-1}, the anodic and cathodic peaks were observed to be symmetric (Figure 9b), suggesting that the VRG350 nanocomposite electrode had excellent reversibility.[34] In addition, the shape of the CV curves with only small distortions showed that VRG350 composites are excellent electron conductors with small equivalent series resistance.[34] However, because of the internal resistance of the electrode, the anodic and cathodic peaks shifted slightly with increasing scan rates.[34,57] Also, we investigated the electrochemical performance of VRG350 at the operation potential window from −1.1 to 0 V (vs Ag/AgCl; see Figure S10 in the Supporting Information).

More accurate galvanostatic charge/discharge tests were also conducted (Figure 9c) to explore the advantages of VRG350 as an electrode material for supercapacitors. The distorted linear shapes imply the operation of pseudocapacitance for the sample of VRG350,[57] which further confirms the results of the CV curves. Figure 9d displayed the relationships between the specific capacitance values and charge/discharge current densities for VRG350 nanocomposites and pure V_2O_5 microspheres. With increasing current densities, their specific capacitance decreased gradually because the diffusion effect confined the migration of the electrolyte ions,[42] leading to a low electrochemical utilization rate of the electrode materials. Over the current density range from 1 to 20 A g^{-1}, the specific capacitance of VRG350 was always higher than that of pure V_2O_5 microspheres. For example, at a current density of 1 A g^{-1}, the specific capacitances of 537 and 202 F g^{-1} were obtained for the samples of VRG350 nanocomposites and pure V_2O_5 microspheres, respectively. When the current density was increased to 20 A g^{-1}, the specific capacitance of the VRG350 electrode was 211.2 F g^{-1}, but it was only 50.2 F g^{-1} for pure V_2O_5 microspheres. This result indicated a good rate capability of VRG350 nanocomposites. Moreover, when measured at a current density of 1 A g^{-1} by a two-electrode system, the specific capacitances of VRG350 nanocomposites and pure V_2O_5 microspheres were 470 and 81 F g^{-1}, respectively (see Figure S11 in the Supporting Information). For VRG350, we also performed its electrochemical performance in a range of potential windows between 0 and 0.8 V, but its specific capacitance was very low (see Figure S12 in the Supporting Information). The above lower capacitance than that of the three-electrode system may occur because the symmetric electrode is commonly not balanced and not optimized, particularly those that are based on Faradaic reactions.[58] It is worth noting that the measured capacitance of VRG350 composites is much higher than that of pure V_2O_5 microspheres (202 F g^{-1} at a current density of 1 A g^{-1}), the previously reported interconnected V_2O_5 nanoporous network (316 F g^{-1} at a current density of 1 A g^{-1}),[20] and PPy@V_2O_5 nanocomposites (308 F g^{-1} at a current density of 0.1 A g^{-1}).[59] As mentioned above, these results further prove that V_2O_5 and rGO in VRG350 nanocomposites have the effect of synergistically enhancing the electrochemical activities.

To further understand their capacitive behaviors, we carried out EIS tests, which are recognized as the foremost method for inspecting the elementary behavior of supercapacitors.[60] In the high-frequency region, the resulting Nyquist plots exhibited semicircles, which imply the existence of charge-transfer resistance (R_{ct}). At low frequency, the slope of the line presented the capacitive character. Compared with pure electrochemical double-layer capacitors, the deviation in the slope (Figure 10a), not the ideal 90° phase angle, might be due

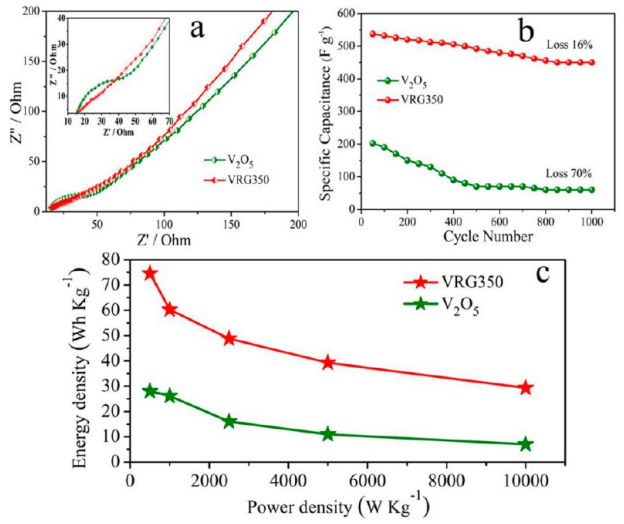

Figure 10. (a) Nyquist plots of experimental impedance. (b) Cycle stability measurement at the current density of 1 A g^{-1}. (c) Ragone plot for VRG350 composites and a pure V_2O_5 electrode.

to a contribution of pseudocapacitance. This substantiated the results of the CV and galvanostatic charge/discharge curves. Differing from a pure V_2O_5 microsphere electrode, the semicircle in the high-frequency range is very small for a VRG350 electrode, manifesting the good conductivity and excellent operation rate of the VRG350 for supercapacitors.

The cycling performance is an important requirement for the application of supercapacitors. The cyclic stability of VRG350 composites and pure V_2O_5 microspheres was examined by means of charge/discharge cycling at a current density of 1 A g^{-1} for 1000 cycles. Figure 10b displays the retention of their discharge capacitance as a function of the number of cycles. The capacitance decreased for both electrode materials initially, while VRG350 nanocomposite electrodes possessed a lower fading effect during charge/discharge cycling compared to pure V_2O_5 microsphere electrodes. For example, the specific capacitance of the VRG350 electrode retained 84% of its initial capacitance, but only 30% was retained for the pure V_2O_5 microsphere electrode after 1000 cycles. This demonstrated that the VRG350 electrode for supercapacitors was more stable toward cycling than that of pure V_2O_5 microspheres. In addition, the power (P) and energy (E) densities are also important parameters for evaluating the electrochemical properties of supercapacitors. Whether the VRG350 electrode is suitable for supercapacitors was further evaluated by examining its power and energy densities. As shown in Figure 10c, its energy density was able to reach 74.58 W h kg^{-1} at a power density of 500 W kg^{-1} and still remained at 29.33 W h kg^{-1} when the power density increased to 10000 W kg^{-1}. These values are higher than that of a pure V_2O_5 electrode and the previously reported V_2O_5-based electrode materials.[17−20] Therefore, the high energy and power densities pave the way for VRG350 nanocomposites as a promising electrode material for supercapacitors in hybrid vehicle systems in the future.

4. CONCLUSION

In summary, highly uniform V_2O_5 nanorods/rGO composites have been successfully prepared as electrode materials for supercapacitors through a facile and efficient strategy. Their structure and electrochemical properties could be controlled by tuning the annealing temperature and vanadium content.

Electrochemical measurements indicated that the VRG350 electrode exhibited a higher specific capacitance (537 F g^{-1}), as well as a higher energy density (74.58 W h kg^{-1}), and better stability than a pure V_2O_5 microsphere electrode. These excellent electrochemical properties were attributed to the synergistic effect of rGO and V_2O_5 nanorods. It is believed that these V_2O_5 nanorods/rGO composites with excellent electrochemical performance can be very promising for high-performance electrode materials in supercapacitors and other energy-storage devices.

■ ASSOCIATED CONTENT

Ⓢ Supporting Information

Additional characterization data (SEM, TEM, HRTEM, XRD, XPS, FTIR, BET, elemental analysis, and electrochemical data). This material is available free of charge via the Internet at http://pubs.acs.org.

■ AUTHOR INFORMATION

Corresponding Authors

*Tel: +86 431 85716671. Fax: +86 431 857164. E-mail: sunguoying@mail.ccut.edu.cn.
*E-mail: klai@ciac.jl.cn.

Notes

The authors declare no competing financial interest.

■ ACKNOWLEDGMENTS

Financial support by the National Natural Science Foundation of China (Grant 21003013) and Changchun Institute of Applied Chemistry, Chinese Academy of Sciences is gratefully acknowledged.

■ REFERENCES

(1) Glushenkov, A. M.; Hulicova-Jurcakova, D.; Llewellyn, D.; Lu, G. Q.; Chen, Y. *Chem. Mater.* **2010**, *22*, 914−921.
(2) Simon, P.; Gogotsi, Y. *Nat. Mater.* **2008**, *7*, 845−854.
(3) Liu, C. G.; Yu, Z. N.; Neff, D.; Zhamu, A.; Jang, B. Z. *Nano Lett.* **2010**, *10*, 4863−4868.
(4) Zhu, Y. W.; Murali, S.; Stoller, M. D.; Ganesh, K. J.; Cai, W. W.; Ferreira, P. J.; Pirkle, A.; Wallace, R. M.; Cychosz, K. A.; Thommes, M.; Su, D.; Stach, E. A.; Ruoff, R. S. *Science* **2011**, *332*, 1537−1541.
(5) Burke, A. *Electrochim. Acta* **2007**, *53*, 1083−1097.
(6) Chmiola, J.; Yushin, G.; Gogotsi, Y.; Portet, C.; Simon, P.; Taberna, P. L. *Science* **2006**, *313*, 1760−1763.
(7) Cheng, Y. W.; Lu, S. T.; Zhang, H. B.; Varanasi, C. V.; Liu, J. *Nano Lett.* **2012**, *12*, 4206−4211.
(8) Kim, I. H.; Kim, J. H.; Cho, B. W.; Lee, Y. H.; Kim, K. B. *J. Electrochem. Soc.* **2006**, *153*, A989−A996.
(9) Hu, C. C.; Chen, W. C.; Chang, K. H. *J. Electrochem. Soc.* **2004**, *151*, A281−A290.
(10) Yan, J.; Khoo, E.; Sumboja, A.; Lee, P. S. *ACS Nano* **2010**, *4*, 4247−4255.
(11) Yue, W. B.; Jiang, S. H.; Huang, W. J.; Gao, Z. Q.; Li, J.; Ren, Y.; Zhao, X. H.; Yang, X. J. *J. Mater. Chem. A* **2013**, *1*, 6928−6933.
(12) Lang, J. W.; Kong, L. B.; Wu, W. J.; Luo, Y. C.; Kang, L. *Chem. Commun.* **2008**, *35*, 4213−4215.
(13) Choi, D.; Blomgren, G. E.; Kumta, P. N. *Adv. Mater.* **2006**, *18*, 1178−1182.
(14) Lu, X. H.; Yu, M. H.; Zhai, T.; Wang, G. M.; Xie, S. L.; Liu, T. Y.; Liang, C. L.; Tong, Y. X.; Li, Y. *Nano Lett.* **2013**, *13*, 2628−2633.
(15) Yang, Y.; Kim, D.; Yang, M.; Schmuki, P. *Chem. Commun.* **2011**, *47*, 7746−7748.
(16) Boukhalfa, S.; Evanoff, K.; Yushin, G. *Energy Environ. Sci.* **2012**, *5*, 6872−6879.
(17) Lao, Z. J.; Konstantinov, K.; Tournaire, Y.; Ng, S. H.; Wang, G. X.; Liu, H. K. *J. Power Sources* **2006**, *162*, 1451−1454.
(18) Reddy, R. N.; Reddy, R. G. *J. Power Sources* **2006**, *156*, 700−704.
(19) Huang, C. M.; Hu, C. C.; Chang, K. H.; Li, J. M.; Li, Y. F. *J. Electrochem. Soc.* **2009**, *156*, A667−A671.
(20) Saravanakumar, B.; Purushothaman, K. K.; Muralidharan, G. *ACS Appl. Mater. Interfaces* **2012**, *4*, 4484−4490.
(21) Coustier, F.; Hill, J.; Owens, B. B.; Passerini, S.; Smyrl, W. H. *J. Electrochem. Soc.* **1999**, *146*, 1355−1360.
(22) Wang, Y.; Takahashi, K.; Lee, K.; Cao, G. Z. *Adv. Funct. Mater.* **2006**, *16*, 1133−1144.
(23) Asim, N.; Radiman, S.; Yarmo, M. A.; Golriz, M. S. B. *Microporous Mesoporous Mater.* **2009**, *120*, 397−401.
(24) Chao, Z. S.; Ruckenstein, E. *Chem. Mater.* **2002**, *14*, 4611−4618.
(25) Liu, J.; Wang, X.; Peng, Q.; Li, Y. *Adv. Mater.* **2005**, *17*, 764−767.
(26) Gu, G.; Schmid, M.; Chiu, P.; Minett, A.; Fraysse, J.; Kim, G.; Roth, S.; Kozlov, M.; Munoz, E.; Bauhgman, R. H. *Nat. Mater.* **2003**, *2*, 316−319.
(27) Pan, A.; Wu, H. B.; Yu, L.; Lou, X. W. *Angew. Chem., Int. Ed.* **2013**, *52*, 2226−2230.
(28) Fasolino, A.; Los, J. H.; Katsnelson, M. I. *Nat. Mater.* **2007**, *6*, 858−861.
(29) Wu, Z. S.; Wang, D. W.; Ren, W.; Zhao, J.; Zhou, G.; Li, F.; Cheng, H. M. *Adv. Funct. Mater.* **2010**, *20*, 3595−3602.
(30) Chen, S.; Zhu, J. W.; Wu, X. D.; Han, Q. F.; Wang, X. *ACS Nano* **2010**, *4*, 2822−2830.
(31) Mini, P. A.; Balakrishnan, A.; Nair, S. V.; Subramanian, K. R. V. *Chem. Commun.* **2011**, *47*, 5753−5755.
(32) Rui, X. H.; Zhu, J. X.; Sim, D. H.; Xu, C.; Zeng, Y.; Hng, H. H.; Lim, T. M.; Yan, Q. Y. *Nanoscale* **2011**, *3*, 4752−4758.
(33) Zhao, H. B.; Pan, L. Y.; Xing, S. Y.; Luo, J.; Xu, J. Q. *J. Power Sources* **2013**, *222*, 21−31.
(34) Yan, J.; Fan, Z. J.; Sun, W.; Ning, G. Q.; Wei, T.; Zhang, Q.; Zhang, R. F.; Zhi, L. J.; Wei, F. *Adv. Funct. Mater.* **2012**, *22*, 2632−2641.
(35) Fan, Z. J.; Yan, J.; Wei, T.; Zhi, L. J.; Ning, G. Q.; Li, T. Y.; Wei, F. *Adv. Funct. Mater.* **2011**, *21*, 2366−2375.
(36) Hummers, W. S.; Offeman, R. E. *J. Am. Chem. Soc.* **1958**, *80*, 1339−1339.
(37) Qu, Q. T.; Liu, L. L.; Wu, Y. P.; Holze, R. *Electrochim. Acta* **2013**, *96*, 8−12.
(38) Sathiya, M.; Prakash, A. S.; Ramesha, K.; Tarascon, J. M.; Shukla, A. K. *J. Am. Chem. Soc.* **2011**, *133*, 16291−16299.
(39) Livage, J. *Solid State Ionics* **1996**, *86*−*88*, 935−942.
(40) Livage, J. *Chem. Mater.* **1991**, *3*, 578−593.
(41) Park, S.; Ruoff, R. S. *Nat. Nanotechnol.* **2009**, *4*, 217−224.
(42) Pan, A. Q.; Zhang, J. G.; Nie, Z. M.; Cao, G. Z.; Arey, B. W.; Li, G. S.; Liang, S. Q.; Liu, J. *J. Mater. Chem.* **2010**, *20*, 9193−9199.
(43) Reddy, C. V. S.; Wicker, S. A.; Walker, E. H.; Williams, Q. L.; Kalluru, R. R. *J. Electrochem. Soc.* **2008**, *155*, A599−A602.
(44) Ibris, N.; Salvi, A. M.; Liberatore, M.; Decker, F.; Surca, A. *Surf. Interface Anal.* **2005**, *37*, 1092−1104.
(45) Deng, L. J.; Zhang, G. N.; Kang, L. P.; Lei, Z. B. *Electrochim. Acta* **2013**, *112*, 448−457.
(46) Akhavan, O.; Abdolahad, M.; Esfandiar, A.; Mohatashamifar, M. *J. Phys. Chem. C* **2010**, *114*, 12955−12959.
(47) Ai, K. L.; Liu, Y. L.; Lu, L. H.; Cheng, X. L.; Huo, L. H. *J. Mater. Chem.* **2011**, *21*, 3365−3370.
(48) Souza, A. G.; Ferreira, O. P.; Santos, E. J. G.; Mendes, J.; Alves, O. L. *Nano Lett.* **2004**, *4*, 2099−2104.
(49) Brousse, T.; Taberna, P. L.; Crosnier, O.; Dugas, R.; Guillemet, P.; Scudeller, Y.; Zhou, Y.; Favier, F.; Belanger, D.; Simon, P. *J. Power Sources* **2007**, *173*, 633−641.
(50) Liu, A.; Ichihara, M.; Honma, I.; Zhou, H. *Electrochem. Commun.* **2007**, *9*, 1766−1771.
(51) Guo, H. L.; Wang, X. F.; Qian, Q. Y.; Wang, F. B.; Xia, X. H. *ACS Nano* **2009**, *3*, 2653−2659.

(52) Zhu, H.; Wang, X. L.; Yang, F.; Yang, X. R. *Adv. Mater.* **2011**, *23*, 2745−2748.
(53) Silversmi, G.; Depla, D.; Poelman, H.; Marin, G. B.; De Gryse, R. *J. Electron Spectrosc. Relat. Phenom.* **2004**, *135*, 167−175.
(54) Perera, S. D.; Patel, B.; Nijem, N.; Roodenko, K.; Seitz, O.; Ferraris, J. P.; Chabal, Y. J.; Balkus, K. J. *Adv. Energy Mater.* **2011**, *1*, 936−945.
(55) Park, S.; Ruoff, R. S. *Nat. Nanotechnol.* **2009**, *4*, 217−224.
(56) Xiao, Y. H.; Liu, S. J.; Li, F.; Zhang, A. Q.; Zhao, J. H.; Fang, S. M.; Jia, D. Z. *Adv. Funct. Mater.* **2012**, *22*, 4052−4059.
(57) Li, H. B.; Yu, M. H.; Wang, F. X.; Liu, P.; Liang, Y.; Xiao, J.; Wang, C. X.; Tong, Y. X.; Yang, G. W. *Nat. Commun.* **2013**, *4*, 1894.
(58) Khomenko, V.; Frackowiak, E.; Beguin, F. *Electrochim. Acta* **2005**, *50*, 2499−2506.
(59) Qu, Q. T.; Zhu, Y. S.; Gao, X. W.; Wu, Y. P. *Adv. Energy Mater.* **2012**, *2*, 950−955.
(60) Sugimoto, W.; Iwata, H.; Yokoshima, K.; Murakami, Y.; Takasu, Y. *J. Phys. Chem. B* **2005**, *109*, 7330−7338.